Acta Cryst. (1996). A52, 686–699

Dynamical Effects of High-Energy Electron Diffraction in Non-centrosymmetric Sphalerite, ZnS

H. MATSUHATA*† AND J. GJØNNES

Department of Physics, University of Oslo, PO Box 1048 Blindern, 0316 Oslo 3, Norway. E-mail: e8917@etlrips.etl.go.jp

(Received 15 May 1995; accepted 2 April 1996)

Abstract

In order to study accidental degeneracies of Bloch waves in non-centrosymmetric crystals, many-beam dynamical effects in high-energy electron diffraction from sphalerite $F\bar{4}3m$ ZnS have been observed. Several critical-voltage effects due to accidental degeneracies, which were created by projected mirror or rotation symmetries, were observed at various crystallographic orientations. Diffraction phenomena very similar to critical-voltage effects were also observed at the non-centrosymmetric projections. These phenomena were discussed using the second Bethe approximation. By the analysis of experimentally measured critical voltages, the structure factors for the 220 and 200 reflections were determined accurately and discussed in terms of the charge rearrangement caused by ionization.

1. Introduction

The atomic scattering factors for electrons are more sensitive to the distribution of outer electrons of an atom than those for X-rays, as is elucidated by the Mott relation,

$$f^{el}(s) = (me^2/2h^2)[Z - f^x(s)]/s^2,$$

where $s = \sin\theta/\lambda$, θ is the Bragg angle, λ is the wavelength of an electron, Z is the atomic number and $f^{el}(s)$ and $f^x(s)$ are the scattering factors for electrons and for X-rays, respectively. This advantage in sensitivity has been exploited through structure-factor refinement based on convergent-beam electron diffraction (for a recent review, see Spence & Zuo, 1992). Measurement and analysis of the critical-voltage effect, which was originally studied in Kikuchi patterns, yield accurate structure factors for low-order reflections (Watanabe, Uyeda & Kogiso, 1968), thus revealing information about the ionic state or bonding charge distribution in crystals. In a recent study, we refined the structure factors for rutile-type SnO_2 by measuring the critical-voltage effect and interpreted the results in terms of the ionized state of the crystal (Matsuhata, Gjønnes & Taftø, 1994). Bonding charge distributions in intermetallic compounds have been determined by Fox & Tabbernor (1991) and Fox (1993) from the critical voltages measured using a high-voltage electron microscope.

Most applications of the critical-voltage effect have been based on measuring systematic rows of reflections, which then restrict the method to high-voltage instruments. By adding the use of Bloch-wave degeneracies in non-systematic diffraction conditions (Gjønnes & Høier, 1971) and at zone-axis orientations (Shannon & Steeds, 1977), a wider range of critical voltages can be measured within the commonly used range of accelerating voltages. The potential for the use of this method would then be increased considerably.

Such an accidental Bloch-wave degeneracy, which defines the condition for a critical voltage, can be derived analytically in the three-beam approximation. The phase invariant, namely $\Phi = \varphi_{-\mathbf{h}} + \varphi_{\mathbf{g}} + \varphi_{\mathbf{h}-\mathbf{g}} = n\pi$, which is in general satisfied for centrosymmetric crystals, is seen to be required for an accidental degeneracy to occur in the three-beam case (*e.g.* see Kambe, 1957; Marthinsen, Matsuhata, Høier & Gjønnes, 1988), where $\varphi_{\mathbf{h}}$ is the phase angle of the structure factor of the reflection **h**. In a previous study, we extended the analysis to a four-beam approximation in which the degeneracy condition is expressed as a relationship between structure factors and excitation errors and is written in the form $C^2 + 4pqt = 0$ (see Appendix *A*). However, for non-centrosymmetric crystals, this relationship is satisfied only in special cases. Examples include when mirror planes or rotation axes of even order are present or when the zone-axis projection is centrosymmetric with negligible influence from higher-order Laue zones. Moreover, Gevers, Serneels & David (1974, 1975) and Serneels, David & Gevers (1975) predicted that, if the deviation from centrosymmetry is small, intensity minima will still appear in a manner similar to the critical-voltage effect. This may be called the *pseudo-critical-voltage effect*.

Here we report the observation of dynamical effects that are responsible for the critical-voltage and pseudo-critical-voltage effects using non-centrosymmetric $F\bar{4}3m$ (No. 216) sphalerite ZnS as a representative

† Present address: Electrotechnical Laboratory, 1-1-4, Umezono, Tsukuba, Ibaraki 305, Japan.

crystal. The sphalerite structure has weak reflections, which depend on the difference between the scattering factors for zinc and sulfur. These reflections are sensitive to the charge transfer from Zn to S, which will be more marked in II–VI semiconductors (*e.g.* ZnS) than in III–V semiconductors.

In this paper, we will begin by surveying the various non-systematic critical-voltage effects and pseudo-critical-voltage effects in sphalerite ZnS, taking into account the symmetry of the crystal and referring to the diffraction conditions for non-systematic critical-voltage effects described in the previous paper (Matsuhata & Gjønnes, 1994). Subsequently, we will discuss the analytical expressions for the dynamical three- and four-beam approximations for the non-centrosymmetric cases. Lastly, we will analyse some of the measured critical voltages using many-beam computations to derive accurate structure factors. The analysis results for the critical voltages will be compared with other results to discuss scattering factors of the ionized state.

2. Experimental procedure

Thin specimens of sphalerite ZnS were obtained by the standard Ar-ion etching of polycrystals. The specimens were observed at the [001], [1$\bar{1}$1], [112], [10$\bar{2}$], [013] and [110] projections. The $F\bar{4}3m$ structure has mirror symmetry about the (110) planes and $\bar{4}$ inversion axes parallel to the ⟨100⟩ directions. The combination of this mirror symmetry with the $\bar{4}$ inversion axes creates various Bloch-wave symmetries, which in turn generate several accidental degeneracies in the above projections. Convergent-beam electron diffraction (CBED) patterns were taken at various accelerating voltages with a minimum step of 1 kV using JEM-2000FX and JEM-4000FX analytical-type electron microscopes. The critical voltages were measured by monitoring the vanishing intensity and the reversal of the asymmetric intensity profiles in the convergent-beam patterns. The accelerating voltage of the 2000FX microscope was calibrated using measurements of Kikuchi-line intersections (Høier, 1969).

Considering up to approximately 250 beams, we carried out many-beam dynamical computation based on the Hermitian diagonalization without considering absorption effects. The symmetries of the Bloch waves were described using the notation introduced by Cochran (1952) and discussed further by Gjønnes & Taftø (1993). The BSW (Bouckaert, Smoluchowski & Wigner) notation introduced by Shannon & Steeds (1977) for Bloch-wave symmetry and the locations in two-dimensional reciprocal space were also used.

The approximate diffraction conditions used in observing the dynamical effects are summarized in Fig. 1, where the dashed-line circles indicate the Laue circles and the dots indicate the reciprocal-lattice points.

3. Experimental results and analysis

3.1. *Dynamical effect at a centrosymmetric zone axis*

3.1.1. *2$\bar{4}$2 reflection at the [111] projection.* Strictly speaking, the symmetry of the zeroth-order Laue zone at the [111] zone axis is $3m$ with the mirror symmetry

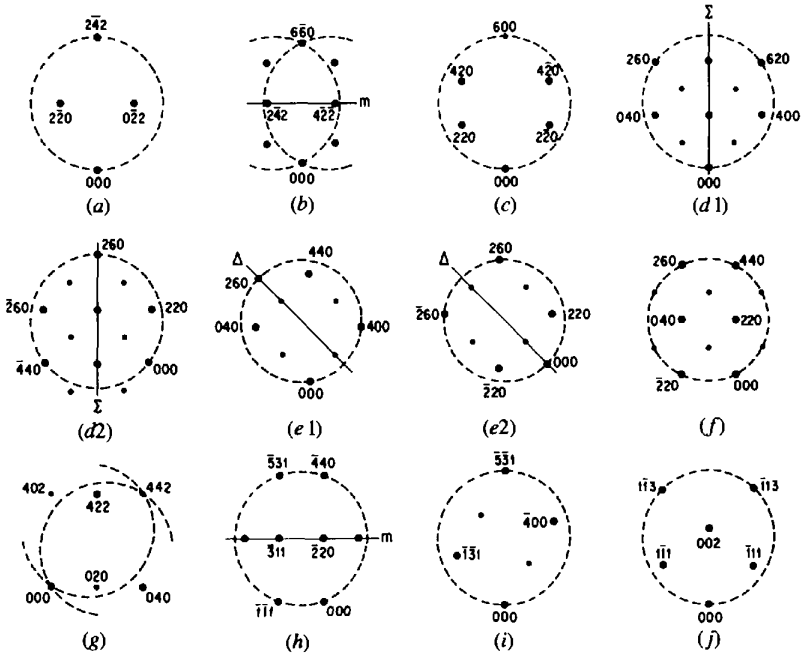

Fig. 1. Approximate diffraction conditions at which various dynamical effects were observed. (*a*) The 2$\bar{4}$2 reflection at the Bragg position at the [111] projection. (*b*) The 66$\bar{0}$ reflection at the Bragg position at the [111] projection. (*c*) The 600 reflection at the Bragg position at the [001] projection. (*d*1) The 260 and 620 reflections near the Bragg position at the [001] projection. (*d*2) The 260 and $\bar{4}$40 reflections near the Bragg position. (*e*1) The 260 and 400 reflections near the Bragg position. (*e*2) The 260 and $\bar{2}$60 reflections near the Bragg position. (*f*) The 260, 440 and $\bar{2}$20 reflections near the Bragg position. (*g*) The 442 reflection near the Bragg position at the [10$\bar{2}$] projection. (*h*) The $\bar{4}$40, $\bar{5}$31 and $\bar{1}$11 at the Bragg position at the non-centrosymmetric [112] projection. (*i*) The $\bar{5}\bar{3}$1 reflection at the Bragg position at the non-centrosymmetric [013] projection. (*j*) The non-systematic pseudo-critical-voltage effect at the [110] projection, where the 1$\bar{1}$3 and $\bar{1}$13 reflections are approximately on the Laue circle.

about the (110) plane. However, this symmetry can be taken to be centrosymmetric *6mm* since the many-beam dynamical calculation shows that the anharmonic contribution to the temperature factors of reflections in the zeroth-order Laue zone is negligible. Fig. 2 shows the non-systematic critical-voltage effect on the $2\bar{4}2$ reflection for the configuration in Fig. 1(*a*) at 102, 142 and 203 kV. A pair of intensity absences, which were due to an accidental degeneracy between Bloch waves 3 and 4, occurred in the $2\bar{4}2$ convergent-beam disc at 102 kV. While one Bloch wave is symmetric (*i.e.* *m*, or Σ_1 in BSW notation) on the Σ line, the other is antisymmetric (*i.e.* *m'* or Σ_2). With increasing accelerating voltage, these points move towards the centre of the $2\bar{4}2$ convergent-beam disc, namely along the Σ line towards the *M* point. The dispersion surfaces show *2mm* symmetry with respect to the *M* point. At 142 kV, the points of intensity absence merge at the *M* point (seen in the centre of the $2\bar{4}2$ disc), corresponding to a degeneracy between the *2mm*- and *2'm'm*-type (or M_1 and M_4) Bloch waves. These symmetries on the *M* point satisfy the compatibility relation with those of the Bloch waves along the Σ lines (see, for example, Burns, 1977). At higher accelerating voltages, the intensity absence is no longer observed (Fig. 2*c*).

Use of a four-beam approximation (Matsuhata & Gjønnes, 1994) gives the positions of the two accidental degeneracy points measured from the *M* point as

$$\delta = \pm\,(1/g)\big(\{\rho^2 - \beta[2a^2 - b^2 - ab)/b]\} \times [\rho^2 - \beta(a-b)]\big)^{1/2}, \quad (1)$$

where $\rho^2 = (h^2 - g^2)/4$, $h = 2\bar{4}2$, $g = \bar{2}02$, $a = U_{2\bar{2}0}$, $b = U_{2\bar{4}2}$ and $\beta = 1 + eE/m_0c^2$. E is the accelerating voltage, m_0 is the electron rest mass, e is the charge of the electron and c is the speed of light. δ is the position parameter of the projected centre of the Ewald sphere onto the zeroth-order Laue zone. The critical voltage E_c at the *M* point is given by

$$E_c = (m_0c^2/e)\{[(b/2a^2 - b^2 - ab)]\rho^2 - 1\}. \quad (2)$$

By measuring either the distance between the two degeneracy points in the convergent-beam disc or the critical voltage at which the degeneracy disappears at the *M* point, we can obtain a relation between the structure factors. Equation (1) indicates that the degeneracy positions become even more sensitive to the structure factor as the degeneracies approach the *M* point. The critical voltage was measured to be 153 (5) kV at the *M* point and was analysed using many-beam dynamical calculations involving 72 beams. Using temperature factors obtained by Cooper, Rouse & Fuess (1973) and higher-order scattering factors obtained by Doyle & Turner (1968), we determined the structure factor for the 220 reflection to be $U_{220} = 0.03822\,(12)\,\text{Å}^{-2}$. This value is 0.7% larger than that calculated from the neutral state by Doyle & Turner (1968).

3.1.2. *$6\bar{6}0$ reflection at the [111] projection.* An accidental degeneracy is observed also in the $6\bar{6}0$, $4\bar{2}\bar{2}$, $2\bar{4}2$, 000 CBED discs in the [111] orientation. The diffraction condition for this accidental degeneracy is shown in Fig. 1(*b*). Fig. 3 shows large-angle convergent-beam diffraction (LACBED) patterns of these reflections taken at 203 kV. The absence in intensity contrast occurred for both the $6\bar{6}0$ and 000 reflections, and the reversal of the asymmetric intensity profile was observed for both the $2\bar{4}2$ and $4\bar{2}\bar{2}$ reflections. The degeneracy is between Bloch waves 9 and 10 on the *T* line. Note that these are exact accidental degeneracies even if the higher-order Laue zones are included, since on the *T* line the Bloch-wave symmetries *m* and *m'* (or T_1 and T_2) are preserved. Using the three-beam approximation introduced by Gjønnes & Høier

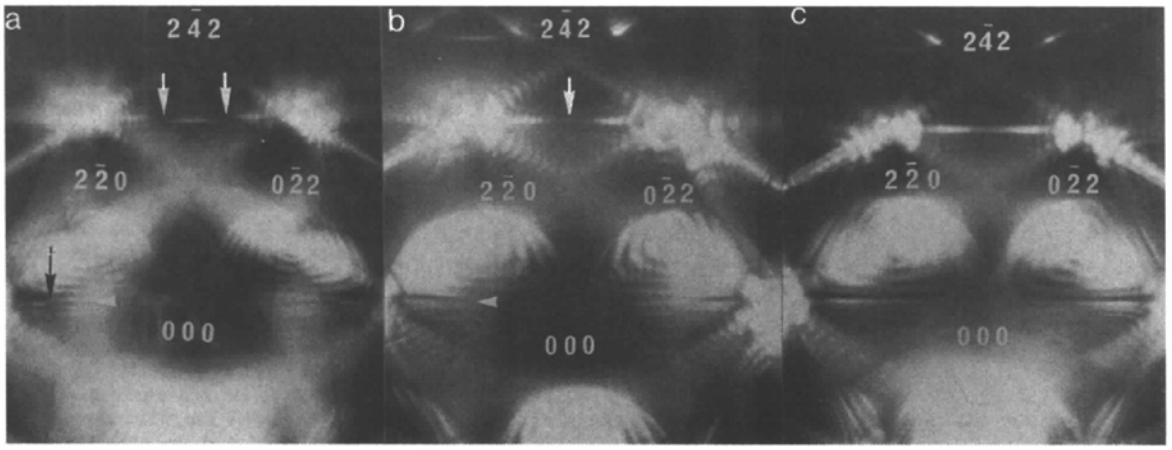

Fig. 2. Non-systematic critical-voltage effect in the $2\bar{4}2$ reflection observed at the [111] zone axis at accelerating voltages of (*a*) 102, (*b*) 142 and (*c*) 203 kV. At 102 kV, the absence in intensity is observed at two different positions. At 142 kV, the points of the intensity absence move to the centre of the $2\bar{4}2$ disc. At 203 kV, the intensity absence disappears. At the corresponding positions in the $2\bar{2}0$ and $0\bar{2}2$ convergent-beam discs, the reversal of the asymmetric intensity profile occurs.

(1971), the diffraction condition for the accidental degeneracy is given by the excitation error $s_{4\bar{2}\bar{2}}$, as follows:

$$s_{4\bar{2}\bar{2}} = (1 + eE/m_0c^2)[(a^2 - b^2)/2Kb], \qquad (3)$$

where $a = U_{422}$, $b = U_{660}$ and K is the absolute value of wave vector of an electron in a crystal. With increasing accelerating voltage, the positions of the accidental degeneracy points move along the T line. Unfortunately, these positions are not sensitive to the structure factors within the voltage range available to conventional electron microscopes.

3.1.3. *600 reflection at the [001] projection.* This projection has a $\bar{4}$ inversion axis and mirror symmetries about the (110) planes. The projected symmetry is $4mm$. We inspected several configurations in this projection to investigate the possibility of structure-factor determination of the weak reflections of $h + k + l = 4n + 2$ type. Fig. 4 shows the LACBED patterns for the 600 reflection taken for the configuration given in Fig. 1(*c*), at 100, 200 and 300 kV. We obtained the critical voltage from the intensity absence at the point indicated by the arrow in Fig. 4. This critical voltage was determined to be 200 (10) kV. The corresponding accidental degeneracy occurs between Bloch waves 7 and 8. Below this critical voltage, the symmetry of Bloch wave 7 is $2mm$ and that of Bloch wave 8 is $2'mm'$ (or X_1 and X_3, respectively, in BSW notation) at the X point. Along the Y line, the Bragg condition is satisfied for the 600 reflection and the Bloch waves have m and m' symmetries (Y_1 and Y_2). At the critical voltage, an interchange of the symmetries takes place at the X point. Above the critical voltage, a pair of accidental degeneracy points is created and moves along the Y lines, with the corresponding reversal of the Bloch-wave symmetries along the Y line owing to the compatibility relation for Bloch-wave symmetry. The accidental degeneracy at the X point is due mainly to the dynamical interactions between the 000, 220, $2\bar{2}0$, 420 $4\bar{2}0$ and 600 reflections. With a six-beam approximation, the eigenvalues for $2mm$ and $2'mm'$ symmetries are given by

$$4K\gamma_{2mm} = 2Ks_A + C + E + B + D - [(2Ks_A + C + E + B - D)^2 + 8(A + B)^2]^{1/2} \qquad (4a)$$

$$4K\gamma_{2'mm'} = 2Ks_A + C - E - B - D - [(2Ks_A + C - E - B + D)^2 + 8(A - B)^2]^{1/2}, \qquad (4b)$$

where s_A is the excitation error of the 220 reflection, $A = \beta U_{220}$, $B = \beta U_{420}$, $C = \beta U_{040}$, $D = \beta U_{600}$, $E = \beta U_{200}$ and $\beta = 1 + eE/m_0c^2$.

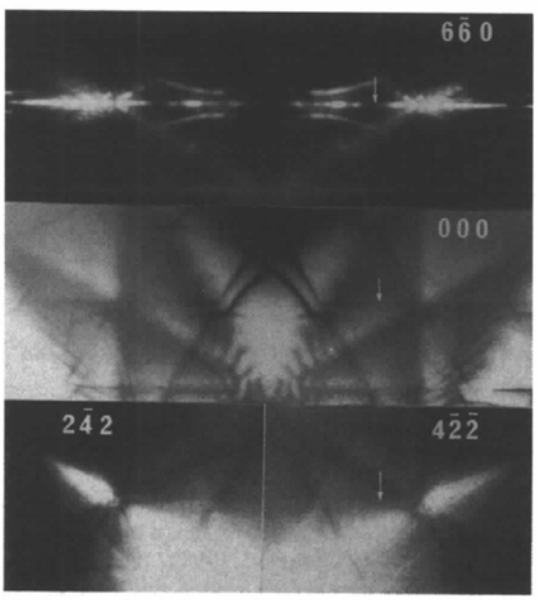

Fig. 3. Accidental degeneracies between Bloch waves 9 and 10 in large-angle convergent-beam patterns of the 6$\bar{6}$0, 2$\bar{4}$2, 4$\bar{2}\bar{2}$ and 000 reflections taken at 203 kV. The intensity absence is observed in the 000 and 6$\bar{6}$0 reflections, and the reversal of the asymmetric intensity profile is observed in the 2$\bar{4}$2 and 4$\bar{2}\bar{2}$ reflections.

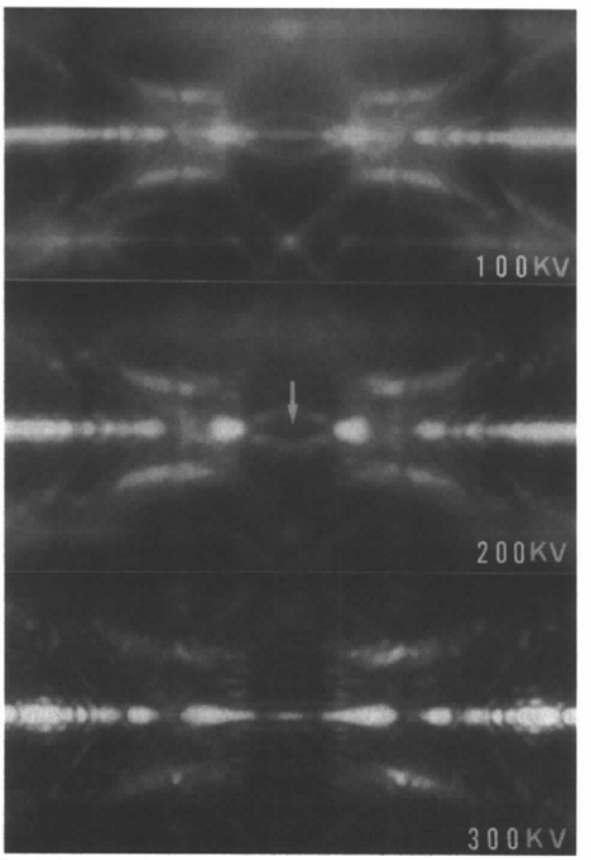

Fig. 4. Large-angle convergent-beam patterns in the 600 reflection for the [001] orientation taken at nominal accelerating voltages of 100, 200 and 300 kV. The arrow indicates the intensity absence.

An accidental degeneracy occurs when the two eigenvalues are equal, *i.e.* $\gamma_{2mm} = \gamma_{2'mm'}$. The six-beam approximation above and also many-beam computations show that this critical voltage depends strongly on the structure factors for the 220 and 420 reflections, and less on those for the 200 and 600 reflections. Many-beam calculations based on the neutral atomic scattering factors by Doyle & Turner (1968) gave a value of 167 kV for the critical voltage at the *X* point. This value is lower than the experimental value of 200 (10) kV. We shall discuss this discrepancy in §5 in terms of the ionization of S and Zn.

3.1.4. *260 reflection at the [001] projection.* A series of intensity absences was observed in the 260 reflection. Fig. 5 shows the bright-field and dark-field LACBED patterns for the [001] zone axis at 102, 203 and 400 kV. Several features in the patterns have characteristics similar to a symmetrical three-beam case (see Kambe, 1957; also Taftø & Gjønnes, 1985). For example, the two split segments marked by *A* and *B* in the patterns are associated with the simultaneous excitation of the 260 and 620 reflections on the Σ line or, alternatively, of the 260 and $\bar{4}40$ reflections. Here, we will discuss mainly the right-hand side of the LACBED patterns for simplicity. The intensity on the opposite side of the dark-field LACBED patterns can be interpreted using the reciprocity theorem in electron diffraction (Pogany & Turner, 1968). The segment *A*, which appears with a weak intensity at 102 kV, originates from Bloch waves 11 and 12. At the intersection with the Σ line, at the position marked by *A'*, these two Bloch waves are degenerate at any accelerating voltage possessing the symmetries *m* and *m'* (or Σ_1 and Σ_2, respectively). The strong intensity in segment *B* is due to the two Bloch waves 9 and 10. These waves both have *m*-type symmetry on the Σ line, but they have opposite signs for $C_0^{(j)*}C_{260}^{(j)}$. When the accelerating voltage was increased to 203 kV, the intensity in segment *A* increased, as seen in Figs. 5(*c*) and (*d*), but an intensity absence owing to an accidental degeneracy occurred in segment *B*.

The non-systematic critical voltage for segment *B* can be expressed analytically using a five-beam approximation, either with the 260 and 620 reflections approximately on the Laue circle and the 040 and $\bar{4}00$ reflections inside the circle or with the 260 and $\bar{4}40$ reflections approximately on the Laue circle and the 220 and $\bar{2}60$ reflections inside the circle for the opposite side of the LACBED pattern. These diffraction conditions are illustrated in Figs. 1(*d*1) and (*d*2). The resulting expression for E_c is

$$E_c = (m_0c^2/e)\big(\{bd(a+d)/[(a+d)^2(2b^2-d^2) - 2b^2d^2 - bcd(a+d)]\}g^2 - 1\big). \quad (5a)$$

The projected position δ_c on the zeroth-order Laue zone for the centre of the Ewald sphere is

$$\delta_c = \big((1+eE/m_0c^2)\{[b(a+d)^2 - cd(a+d) - 2bd^2] \times [2d(a+d)]^{-1}\}(1/g^2) + 1\big)\mathbf{g}, \quad (5b)$$

where $a = U_{220}$, $b = U_{400}$, $c = U_{440}$, $d = U_{620}$ and $\mathbf{g} = \mathbf{g}_{220}$.

Many-beam dynamical computations show that this critical-voltage effect creates a pair of movable accidental degeneracy points between Bloch waves 9 and 10 on the *B* segment. The direction of motion of the accidental degeneracy points with increasing voltage around this critical voltage is illustrated by the arrows in Fig. 5(*g*). Above this critical voltage, one of the accidental degeneracy points moves along the *B* segment of the 260 reflection and reaches the 400 line at the point marked by the solid square in Fig. 5(*h*). The structure of the three-beam dispersion surface around the 400 line, owing to simultaneous excitation of the 260 and 400 reflections, is similar to that around the Σ line discussed above. An accidental degeneracy always exists at the point *B'* between the branches of symmetries *m* and *m'* (Δ_1 and Δ_2). The moving accidental degeneracy point is incorporated into this accidental degeneracy point.

A further increase in the accelerating voltage causes an intensity absence within segment *C* as shown in Figs. 5(*e*) and (*f*). This critical-voltage effect at the intersection with the 400 line is again due to the degeneracy between the two symmetric Bloch waves but their signs for $C_0^{(j)*}C_{260}^{(j)}$ are opposite. This accidental degeneracy can be determined analytically using a five-beam approximation, either with the 260 and 400 reflections approximately on the Laue circle and the 040 and 440 reflections inside the circle or with the 260 and $\bar{2}60$ reflections approximately on the Laue circle and the 220 and $\bar{2}20$ reflections inside the circle for the left-hand side of the LACBED pattern. The diffraction conditions are shown in Figs. 1(*e*1) and (*e*2). The resulting expressions for E_c and for the projected position of the centre of the Ewald sphere are given by

$$E_c = (m_0c^2/e)\big(\{4ad(b+c)/[(b+c)^2(3a^2-d^2) - 4a^2d^2 - 2abd(b+c)]\}h^2 - 1\big), \quad (6a)$$

$$\delta_c = \big((1+eE/m_0c^2)\{[a(b+c)^2 - bd(b+c) - 2ad^2] \times [2d(b+c)]^{-1}\}(1/h^2) + 1\big)\mathbf{h}, \quad (6b)$$

where $a = U_{220}$, $b = U_{400}$, $c = U_{440}$, $d = U_{620}$ and $\mathbf{h} = \mathbf{g}_{020}$.

The diffraction geometry for this critical-voltage effect is similar to that observed in Cu at the [001] zone axis (Matsuhata & Gjønnes, 1994). The direction of motion of degeneracy points around this critical voltage with increasing accelerating voltage is shown schematically in Fig. 5(*h*). Many-beam calculations indicate that one of the pair of degeneracy points moves along the *C* segment towards the centre of the convergent-

beam pattern of the 260 reflection. The corresponding diffraction condition is shown in Fig. 1(*f*), where the 260, 440 and $\bar{2}20$ reflections are excited simultaneously. A high-voltage microscope is required to observe the accidental degeneracy at the central part of the CBED pattern. The intensity absences in segments *A*, *B* and *C* of the 260 LACBED patterns in Fig. 5 show how the accidental degeneracy points move around the 4*mm* symmetry [00$\bar{1}$] zone axis.

3.1.5 *[10$\bar{2}$] projection*. We have examined the influence of weak reflections of the $h+k+l=4n+2$ type on accidental degeneracies at various projections.

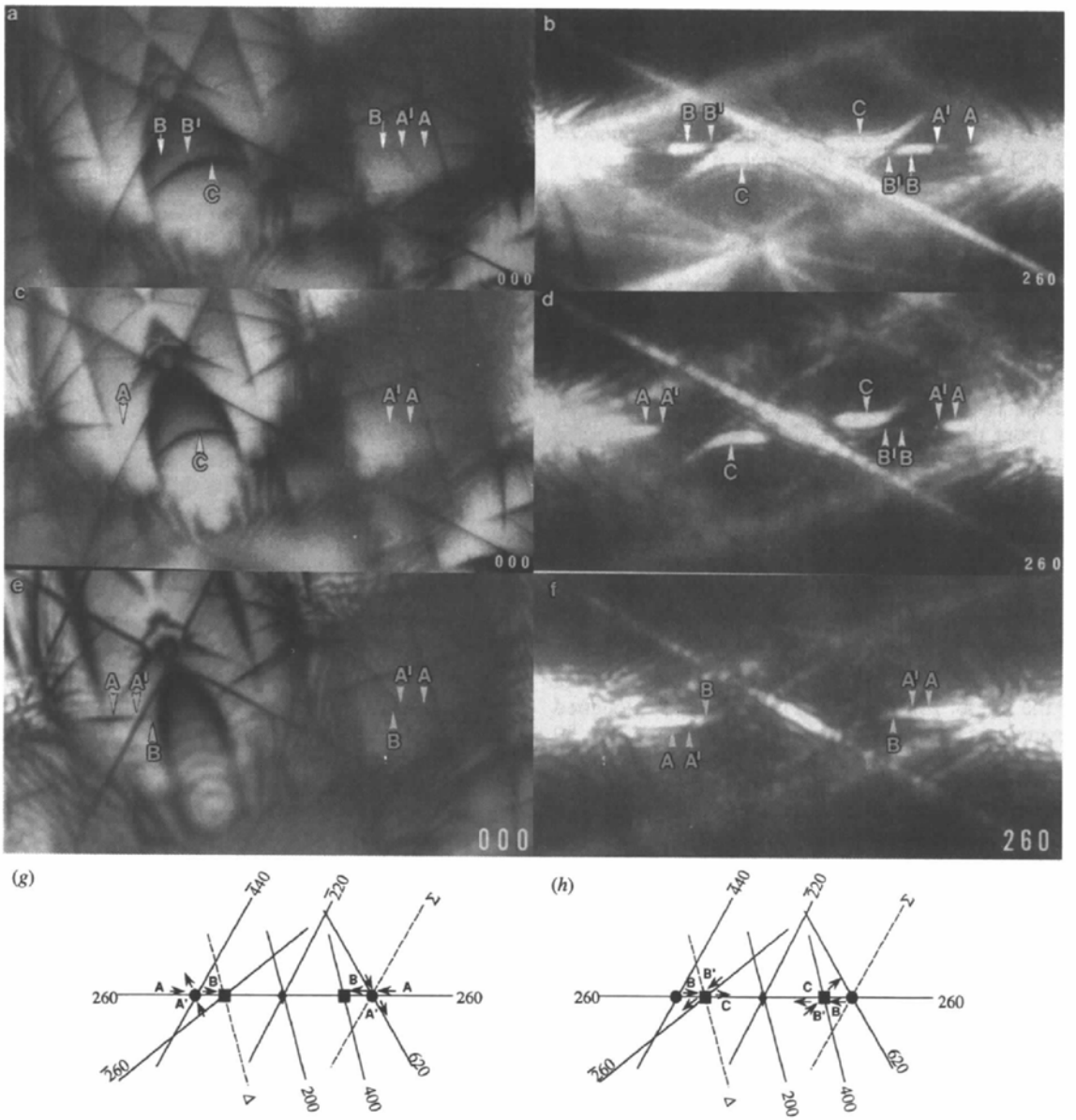

Fig. 5. Bright-field and 260 dark-field large-angle convergent-beam patterns taken at 102 kV (*a* and *b*, respectively), at 203 kV (*c* and *d*, respectively) and nominally at 400 kV (*e* and *f*, respectively) in the [001] zone axis. *A*, *B* and *C* in the figures denote the intensity segments of the 260 reflection. The letters with a prime indicate the locations of absence in contrast owing to an accidental degeneracy, which occurs at any accelerating voltage between *m*-type and *m*′-type Bloch waves. The absences in intensity contrast owing to moving accidental degeneracies are seen in segment *A* at 102 kV, in segment *B* at 203 kV and in segment *C* at 400 kV. (*g*) Intensity segment map of the corresponding region of the 260 LACBED pattern. The directions of motion of accidental degeneracies around the first critical voltage is indicated by arrows. The parts of the 260 intensity segments are denoted by *A* and *B*. The solid circles denoted by *A*′ are the points where the accidental degeneracies are located for any accelerating voltage. (*h*) The direction of motion of accidental degeneracies around the second critical voltage. The parts of the 260 intensity segments are denoted by *B* and *C*. The solid squares denoted by *B*′ are the points where the accidental degeneracies are located for any accelerating voltage.

The effect was anticipated at the [10$\bar{2}$] projection, in which h, k and l are all even for reflections in the zeroth-order Laue zone. Fig. 6 shows a pair of intensity absences in the 442 LACBED pattern at the [10$\bar{2}$] projection associated with accidental degeneracy. The 422, 020 and 442 reflections shown in Fig. 1(g) play an important role for the dynamical interaction, where the 020 and 442 are weak reflections of the $h+k+l=4n+2$ type. With increasing accelerating voltage, these degeneracy points move towards the centre of the 442 convergent-beam pattern. The position of the degeneracy points can be described by equations similar to (3). This accidental degeneracy is influenced by the 020 weak reflection. However, it does not give a satisfactorily accurate U_{200} value in this accelerating range. A more accurate value may be obtained using higher accelerating voltages.

3.2. *Dynamical effect at a non-centrosymmetric zone axis*

3.2.1. *[112] projection.* Even though the [112] projection is non-centrosymmetric, it has mirror symmetry about the ($\bar{1}$10) plane. Thus, when the projected centre of the Ewald sphere is on the Σ line or on the C line, Bloch waves can still be classified as being m or m'. Accidental degeneracies between these different types of Bloch waves (*i.e.* m or m') occur. Fig. 7 shows the absence in intensity in both the $\bar{5}31$ and $\bar{4}40$ CBED patterns under the [112] projection at 82 kV. The diffraction condition for this degeneracy is shown in Fig. 1(h). The $\bar{5}31$, $\bar{4}40$ and $\bar{1}\bar{1}1$ reflections are on the Laue circle. The $\bar{4}02$, $\bar{3}11$, $\bar{2}20$ and $\bar{1}3\bar{1}$ reflections are inside the circle. Figs. 8(a) and (b) show the calculated dispersion surfaces for Bloch waves 5, 6, 7 and 8 at 50 and 120 kV, respectively, along the Σ lines, the X point being in the middle. The accidental degeneracy between Bloch waves 7 and 8 occurs at the X point at 50 kV, and that between Bloch waves 5 and 6 occurs at 70 kV. The CBED discs in Fig. 7 were taken at the voltage above the two critical voltages. The Bloch waves can be characterized by their symmetry, namely m or m' along the Σ line, and m^* or $m^{*\prime}$ along the D line (for this notation see Kästner, 1987). We may introduce symmetric symbols such as $2^*m'm^*$ to describe Bloch waves at the X point. However, we shall only apply the labelling m', m, m' and m to Bloch waves 5, 6, 7 and 8 for the case of 120 kV, respectively, since the use of m^* or $m^{*\prime}$ also depends on how one normalizes the eigenvectors. To the left-hand side of the X point in the $\bar{4}40$ disc, the main intensity contributions come from Bloch waves 5 and 6, whereas Bloch waves 7 and 8 are important for the right-hand side. The intensity absence on the left-hand side is mainly associated with the accidental degeneracy between Bloch waves 5 and 6, while that on the right-hand side results from the accidental degeneracy between Bloch waves 7 and 8. In the $\bar{5}31$ pattern, all four Bloch waves contribute symmetrically about the X point. The many-beam dynamical calculations indicate that the degeneracy between Bloch waves 5 and 6 at the X point depends mainly on U_{220} and U_{440}, whereas the degeneracy between Bloch waves 7 and 8 depends strongly on U_{311} as well. Both critical voltages depend weakly on U_{111}. The influence of the antisymmetric component of the anharmonic temperature factors estimated by Moss, McMullan & Koetzle (1980) on these critical voltages is concluded to be negligible by the dynamical computations.

3.2.2. *[013] projection.* The projection along the [013] zone axis is neither centrosymmetric nor mirror symmetric. Hence, the four-dimensional dynamical matrix cannot satisfy the degeneracy condition $C^2+4pqt=0$. However, an intensity weakening in the $\bar{5}\bar{3}1$ reflection is apparent in Fig. 9 at the diffraction condition shown in Fig. 1(i). When the accelerating voltage was increased, a pair of weak intensity points moved towards the centre of the $\bar{5}\bar{3}1$ CBED disc, then combined there and disappeared. This appearance is very similar to the critical-voltage effect but the Bloch-

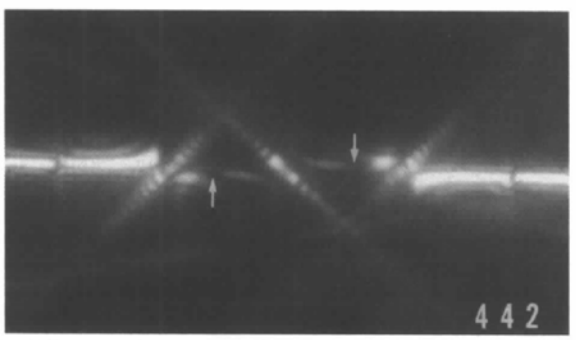

Fig. 6. Large-angle convergent-beam pattern on the 442 reflection for the [10$\bar{2}$] projection taken nominally at 350 kV at the diffraction condition shown in Fig. 1(g). The arrows indicate the intensity absence.

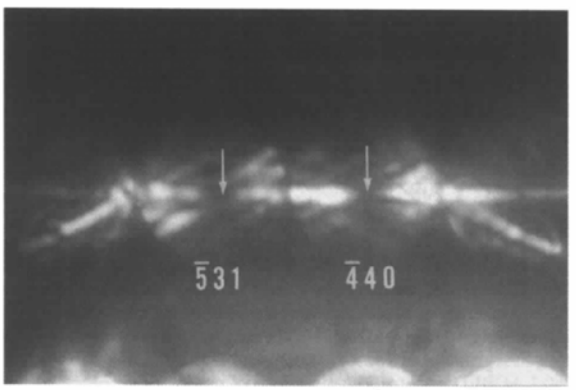

Fig. 7. Convergent-beam patterns of the $\bar{5}31$ and $\bar{4}40$ reflections observed at 82 kV for the [112] orientation for the diffraction condition shown in Fig. 1(h). The arrows indicate the intensity absence.

wave branches do not touch because of the non-centrosymmetry (Gevers *et al.*, 1974, 1975; Serneels *et al.*, 1975). Therefore, this may be called a pseudo-critical-voltage effect.

In this case, the $\bar{4}00$, $\bar{1}\bar{3}1$ and $\bar{5}\bar{3}1$ reflections play an important role in the dynamical interaction. The structure factors of all these reflections, except the 400 reflection, are complex numbers. With Doyle & Turner's (1968) neutral scattering factors, the phase invariant Φ for the three beams, either among the 000, $\bar{1}\bar{3}1$ and $\bar{5}\bar{3}1$ reflections or among the 000, $\bar{4}00$ and $\bar{5}\bar{3}1$ reflections, is given by $\varphi_{\bar{1}\bar{3}1} + \varphi_{\bar{4}00} + \varphi_{53\bar{1}} = 2.035\pi$, which is nearly equal to 2π. Therefore, an appearance similar to that of the critical-voltage effect is observed.

Many-beam dynamical computations show that with an increasing accelerating voltage a pair of the small gap points of the dispersion-surface branches between Bloch waves 5 and 6 moves along the intensity segment of the $\bar{5}\bar{3}1$ reflection towards the centre of the $\bar{5}\bar{3}1$ CBED disc. A pair of the small gap points combines there and disappears. The calculated results show that the interchanges between the magnitudes of the excitation amplitudes and between the absorption parameters of the two Bloch-wave branches occur at the centre part of the $\bar{5}\bar{3}1$ CBED disc. However, there is no contact between the dispersion surfaces of Bloch wave branches 5 and 6. The diffraction condition at the centre of the $\bar{5}\bar{3}1$ CBED disc corresponds to the situation that the projected centre of the Ewald sphere is at the 2* point. A theoretical pseudo-critical voltage can be defined as being the accelerating voltage at which the gap between the two Bloch-wave branches becomes minimal at the 2* point. With this definition, the pseudo-critical voltage is calculated to be 269 kV.

Since there is no degeneracy between the two branches of the dispersion surfaces in the case of the pseudo-critical-voltage effect, the diffracted intensity around the small gap positions of the dispersion surfaces depends also on the crystal thickness. Computer fitting of the experimental rocking curves together with energy filtering of the diffracted electron beam can be used to obtain accurate values for the structure factors.

3.2.3. *[110] projection.* Buxton, Loveluck & Steeds (1978) predicted a critical voltage on the Δ line at the [110] projection for centrosymmetric Si. This critical-voltage effect was observed by Matsuhata & Steeds (1986) for the diffraction condition in which the $1\bar{1}3$ and $\bar{1}13$ reflections were approximately on the Laue circle. At this critical voltage, the accidental degeneracy occurs between Bloch waves 4 and 5. When the projected centre of the Ewald sphere is on the Δ line, both Bloch waves

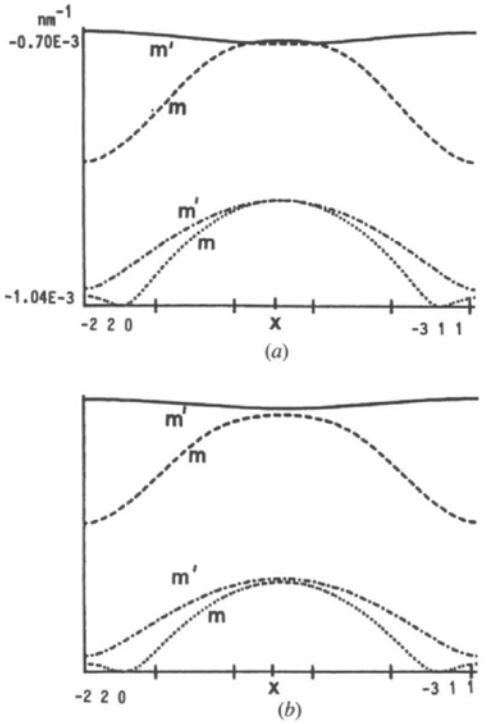

Fig. 8. Calculated dispersion surfaces of Bloch waves 5, 6 7 and 8 along the Σ line (along the $\bar{4}40$ Bragg position) with the X point in the middle of the Σ line at (*a*) 50 kV and (*b*) 120 kV. The solid line, dashed line, dot-dashed line and dotted line indicate Bloch waves 5, 6, 7 and 8, respectively.

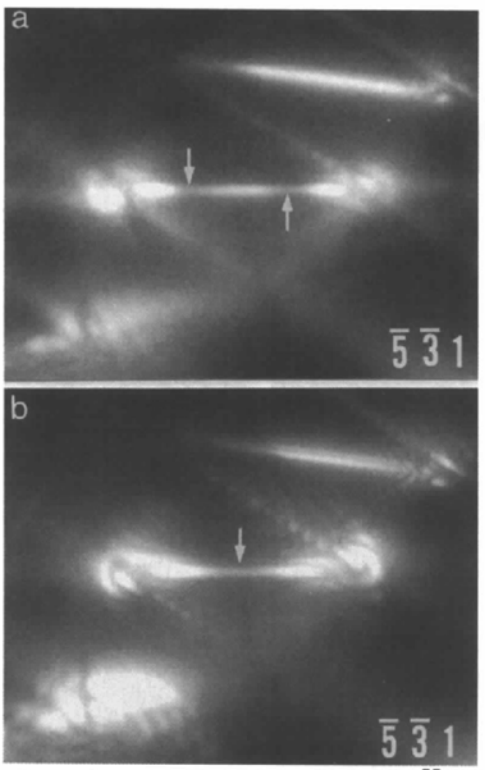

Fig. 9. Observed pseudo-critical-voltage effect on the $\bar{5}\bar{3}1$ reflections at the [013] projection at (*a*) 102 kV and (*b*) nominally at 280 kV. The arrows indicate intensity minima.

have symmetry m but they have opposite signs for $C_0^{(j)*}C_{1\bar{1}3}^{(j)}$. Many-beam dynamical computations show that with increasing voltage a pair of accidental degeneracy points moves in a region of general points, reaches the Δ line, combines there and disappears.

An appearance similar to that of the critical-voltage effect in Si is observed in the LACBED patterns of ZnS at the [110] projection. The patterns in Fig. 10 were taken at 82, 102, 122 and 142 kV. Reversal in the asymmetric intensity profile occurred in both the bright-field and the 002 and $00\bar{2}$ dark-field patterns at the positions indicated by the arrows. In ZnS, the [110] projection has a $(2\bar{2}0)$ mirror plane. When the projected centre of the Ewald sphere is on the Δ line, Bloch waves can be classified as being m or m' in symmetry. However, they are not m or m' on the Σ line, since (002) is not a mirror plane. This pseudo-critical-voltage effect originates from the absence of mirror symmetry in the (002) plane. Fig. 11 shows the dispersion surfaces and excitation amplitudes for the two Bloch waves corresponding to the patterns shown in Fig. 10 and indicates no degeneracy between the two dispersion surfaces. Bloch waves 4 and 5 are of symmetry m on the Δ line but the $C_0^{(j)*}C_{1\bar{1}3}^{(j)}$ for $j = 4$ and 5 are complex numbers.

4. Dynamical effects in non-centrosymmetric crystals

4.1. *Dynamical effect in a systematic three-beam case*

Quantitative analysis of the observed critical-voltage effects relies on many-beam dynamical computations. However, a qualitative discussion of the dynamical effect in relation to non-centrosymmetric cases may be obtained from approximate analytical expressions. The perturbation expressions derived by Gevers *et al.* (1974, 1975) for the critical-voltage effect in non-centrosymmetric crystals appear somewhat cumbersome. Here, we shall apply the second Bethe approximation to some simple non-centrosymmetric cases. (For a discussion on the range of the validity of the approximation, see Zuo, Høier & Spence, 1989.)

In the dynamical effect of a systematic three-beam case with the second-order reflection at the Bragg position, the second Bethe approximation reduces the three-beam dynamical matrix to a quasi-two-beam matrix given by

$$\begin{bmatrix} -\beta^2|U_g|^2/g^2 - 2K\gamma & \beta U_{-2\mathbf{g}} - \beta^2 U_{-\mathbf{g}}^2/g^2 \\ \beta U_{2\mathbf{g}} - \beta^2 U_{\mathbf{g}}^2/g^2 & -\beta^2|U_g|^2/g^2 - 2K\gamma \end{bmatrix}, \quad (7)$$

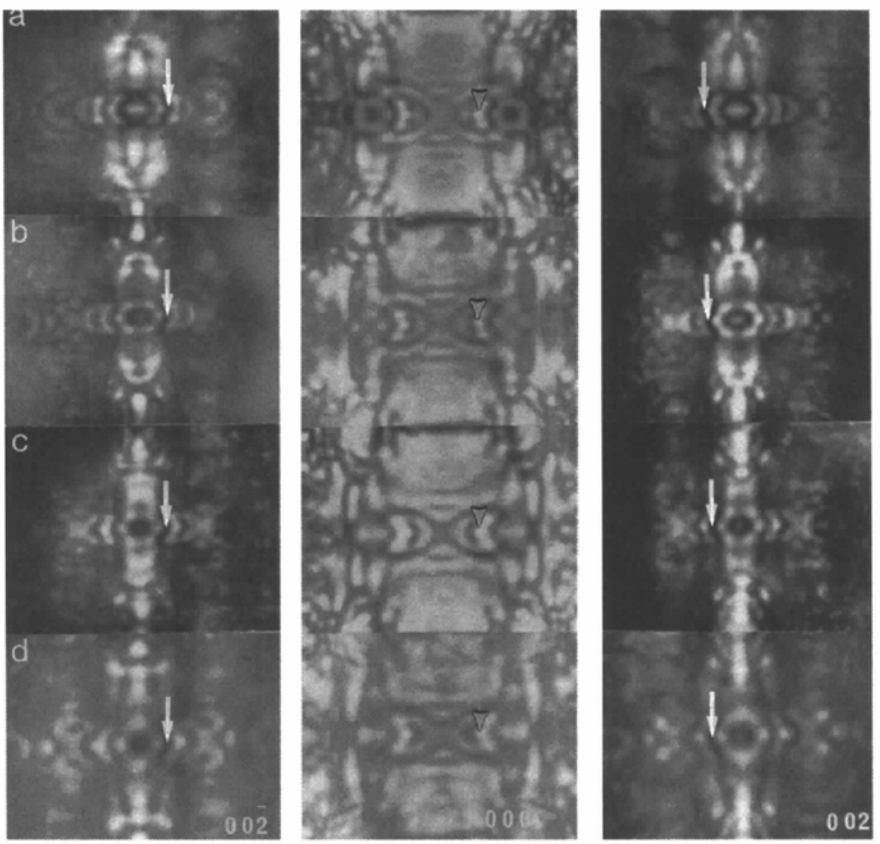

Fig. 10. Observed pseudo-critical-voltage effect at the [110] zone axis. The LACBED patterns were taken at (*a*) 82, (*b*) 102, (*c*) 122 and (*d*) 142 kV. The left column shows the $00\bar{2}$ dark-field, the middle column shows the bright-field, and the right column shows the 002 dark-field patterns.

where β is the relativistic correction factor. The eigenvalues $2K\gamma$ in (7) for the two Bloch waves are given by

$$2K\gamma = -\beta^2|U_g|^2/g^2 \pm [(\beta U_{-2g} - \beta^2 U_{-g}^2/g^2) \times (\beta U_{2g} - \beta^2 U_g^2/g^2)]^{1/2}. \quad (8)$$

The corresponding eigenvectors can be written in matrix form as

$$\begin{bmatrix} A & A\exp(-i\theta) \\ A\exp(i\theta) & -A \end{bmatrix},$$

where

$$\theta = \arg(\beta U_{2g} - \beta^2 U_g^2/g^2) = \arctan[|U_{2g}|\sin\Phi/(|U_{2g}|\cos\Phi - \beta|U_g|^2/g^2)] + 2\varphi_g. \quad (9)$$

$\Phi = \varphi_{2g} - 2\varphi_g$ is a phase invariant of the three reflections, where φ_g is a phase angle of a structure factor for the reflection **g**. For simplicity, φ_g can be taken to be zero by choosing an appropriate origin for the unit cell. If we normalize the eigenvectors by assuming the two-beam approximation, A becomes $1/(2)^{1/2}$. The three-beam normalization condition may be written by expressing C_g as $-(U_gC_0 + U_{-g}C_{2g})/g^2$.

In centrosymmetric crystals, $U_g = U_{-g}$, $U_{2g} = U_{-2g}$, and $\theta = 0$ or π. Accidental degeneracy occurs when off-diagonal elements in the two-dimensional matrix given by (7) are zero. The critical voltage E_c is given by

$$E_c = (m_0c^2/e)[(U_{2g}/U_g^2)g^2 - 1]. \quad (10)$$

Although E_c in (10) derived using the second Bethe approximation is lower than E_c calculated using the exact three-beam case (see, for example, Spence & Zuo, 1992), in what follows we shall use this approximation in our discussion for simplicity.

As can be seen from (9), below the critical voltage the eigenvector components C_0 and C_{2g} belonging to the lower dispersion surface branch have opposite signs, which corresponds to an antisymmetric Bloch wave, whereas the two components of the upper branch have the same sign, which corresponds to a symmetric Bloch wave. Above the critical voltage, this symmetry relation is reversed.

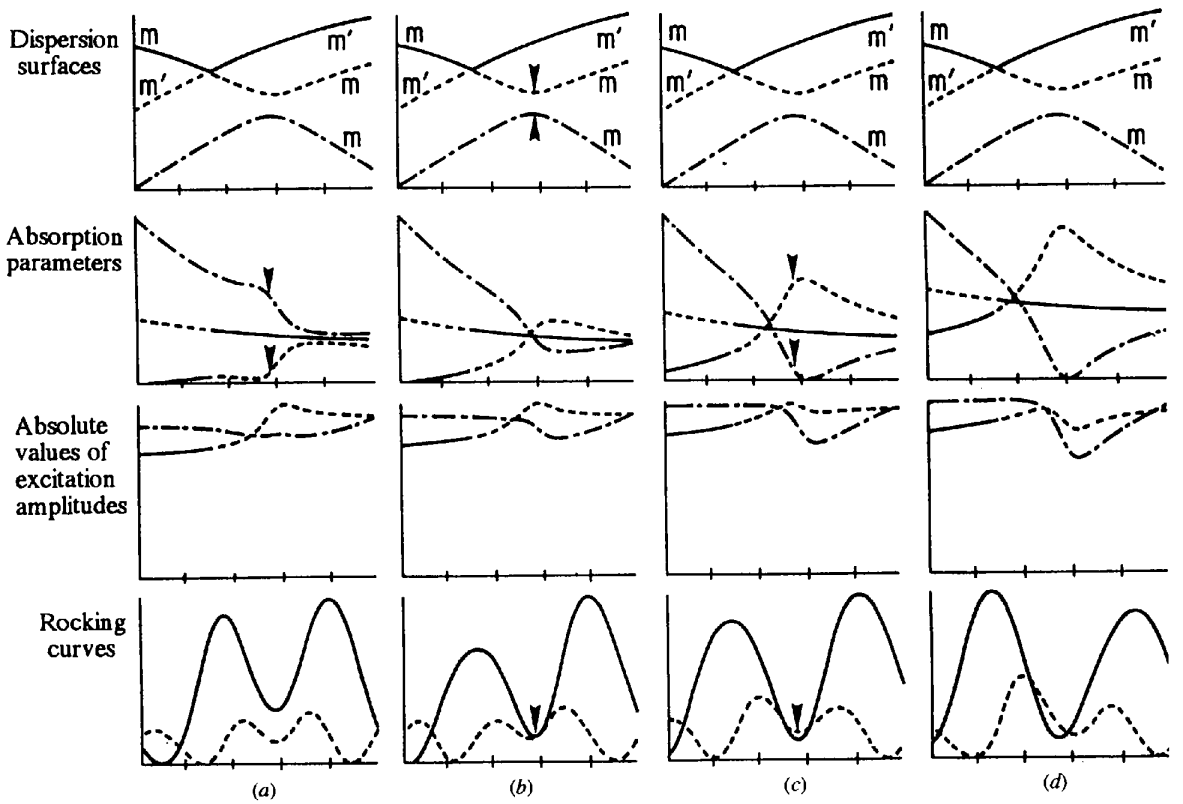

Fig. 11. Calculated dispersion surfaces, absorption parameters, excitation amplitudes and rocking curves for crystal thickness of 200 nm (solid lines) and 300 nm (dashed lines) for thickness along the Δ line at (*a*) 85, (*b*) 95, (*c*) 105 and (*d*) 115 kV for the pseudo-critical voltage observed at the [110] projection. Solid lines, dashed lines and dash-dotted lines correspond to Bloch waves 3, 4 and 5, respectively. The calculations included 114 beams. An arrow on the dispersion-surface curve shows the location of the pseudo-critical voltage. Arrows on the absorption-parameter curves show the interchange of absorption parameters. Arrows on the rocking curves show the intensity-minima positions.

In non-centrosymmetric crystals, $U_{\mathbf{g}}^* = U_{-\mathbf{g}}$ and $U_{2\mathbf{g}}^* = U_{-2\mathbf{g}}$. If Φ is small or near $2n\pi$, the minimum gap between two Bloch-wave branches occurs at the accelerating voltage E_{mg} given by

$$E_{mg} = (m_0c^2/e)\{\{[3|U_{2g}|\cos\Phi + |U_{2g}|(1 - 9\sin^2\Phi)^{1/2}] \times (4|U_g|^2)^{-1}\}g^2 - 1\}. \quad (11)$$

According to this equation, as Φ increases, E_{mg} decreases and the minimum gap becomes more shallow. E_{mg} will eventually vanish when the quantity within the square root in (11) becomes negative. This equation shows that E_{mg} depends on the phase invariant Φ.

Let us consider the Bloch-wave symmetry around the minimum gap of the dispersion surface. The variation of the denominator in the argument of the arctan in (9) around the pseudo-critical voltage corresponds to the reversal of Bloch-wave symmetry in the centrosymmetric case. In the non-centrosymmetric case, as the voltage increases, the term $|\arg(C_0^{(j)*}C_{2\mathbf{g}}^{(j)})|$ for the lower branch decreases but that for the upper branch increases. The denominator in the argument of the arctan in (9) decreases and becomes zero at $\beta = g^2|U_{2g}|\cos\Phi/|U_g|^2$, resulting in $\theta = \pi/2$. The change in the character of the Bloch waves corresponds to a change in the arctan around $\theta = \pi/2$. The accelerating voltage at which the change of the Bloch-wave character takes place is slightly different from E_{mg}. If we take an arbitrary origin for the unit cell, $\varphi_{\mathbf{g}}$ in (9) is not zero. The change in θ occurs similarly to the case for $\varphi_{\mathbf{g}} = 0$ but θ is no longer $\pi/2$ when $\beta = g^2|U_{2g}|\cos\Phi/|U_g|^2$.

4.2. *Non-systematic case*

Let us now discuss a non-systematic four-beam case for a non-centrosymmetric crystal with the skew-diamond configuration, which has been treated previously for the centrosymmetric case (Matsuhata & Gjønnes, 1994). If we assume that the reflection **h** is at the Bragg condition, the reflections **a** and **b** inside the Laue circle will have the same excitation error. Even when there is no twofold rotation axis in the projection, the structure of the dispersion surface will have twofold rotation symmetry. If the reflections **a** and **b** are weakly excited, we may apply the second Bethe approximation and reduce the matrix to the two-beam form

$$\begin{bmatrix} (-\beta^2/\rho^2)(|U_a|^2 + |U_b|^2) - 2K\gamma & \beta U_{-\mathbf{h}} - 2\beta^2 U_{-\mathbf{a}}U_{-\mathbf{b}}/\rho^2 \\ \beta U_{\mathbf{h}} - 2\beta^2 U_{\mathbf{a}}U_{\mathbf{b}}/\rho^2 & (-\beta/\rho^2)(|U_a|^2 + |U_b|^2) - 2K\gamma \end{bmatrix}, \quad (12)$$

where $\rho^2 = (h^2 - g^2)/4$ and $\mathbf{g} = \mathbf{a} - \mathbf{b}$. The non-systematic critical voltage E_c for a centrosymmetric crystal is then given by

$$E_c = (m_0c^2/e)[(U_h/2U_aU_b)\rho^2 - 1]. \quad (13)$$

The eigenvector matrix can be expressed by a matrix similar to (9). For centrosymmetric crystals, an interchange between the Bloch waves that have symmetries 2 and 2′ occurs at the critical voltage in a manner similar to the systematic case. Equation (13) predicts a considerably lower value than the exact four-beam solution. However, for simplicity, we will apply the second Bethe approximation.

In a non-centrosymmetric crystal, the accelerating voltage to achieve the minimum gap between the two Bloch-wave dispersion surfaces is similar to the systematic case,

$$E_{mg} = (m_0c^2/e)\{\{[3|U_h|\cos\Phi + |U_h|(1 - 9\sin^2\Phi)^{1/2}] \times (8|U_a||U_b|)^{-1}\}\rho^2 - 1\}. \quad (14)$$

If we take $\varphi_{\mathbf{a}}, \varphi_{\mathbf{b}} = 0$ for the phases of structure factors for the reflections **a** and **b** by choosing an appropriate origin for the unit cell, the accelerating voltage at which the change in Bloch-wave character occurs can be described in a manner similar to the systematic three-beam case,

$$E = (m_0c^2/e)[(|U_h|\cos\Phi/2|U_a||U_b|)\rho^2 - 1]. \quad (15)$$

It should be noted that the pseudo-critical-voltage value defined by the minimum gap between the dispersion surfaces is different from the accelerating voltage at which the characters of the Bloch waves change.

5. Rearrangement of the outer electrons

In this section, we shall discuss the numerical analysis of the critical voltages measured experimentally. Of the crystal settings for observation of critical voltages shown in Fig. 1, the two cases (*a*) and (*c*) were used to determine the structure factors. We shall interpret these measured critical voltages in terms of the rearrangement of the outer electrons of the constituent atoms. This can be done in several ways: by comparison with theoretical calculations of the electronic structure of the crystal, by comparison with spherically symmetric scattering factors for ionized states or by obtaining adequate structure factors from X-ray diffraction experiments through constructing charge-density maps. Since we have two independent measurements, we shall use the first two approaches, concentrating on the determination of the ionic state.

In theoretical calculations, it is known that the wave functions of outer electrons for isolated negative ions expand and are unstable, particularly for the doubly ionized negative state (see, for example, Schmidt & Weiss, 1979; Azavant & Lichanot, 1993). A crystal potential or an artificial potential is required. The effect of the potentials, therefore, appears in the calculated wave functions of the electrons. Fig. 12 shows the change in scattering factors for electrons due to ionization obtained from different models. The

curve for S^{2-} denoted by $\kappa = 0.91$ was obtained using a model by Coppens *et al.* (1979) and Coppens (1993). Using the phenomenological parameter κ, the contraction or expansion of the spherically symmetric distribution of the outer electrons can be considered. The X-ray scattering factor of S^{2-} is expressed as $f^X_{S^{2-}}(\sin\theta/\lambda) = f^X_{\text{Ne-core}}(\sin\theta/\lambda) + 2f^X_{3s\text{-electron}}(\sin\theta/\kappa\lambda) + 6f^X_{3p\text{-electron}}(\sin\theta/\kappa\lambda)$, and can then be converted to an electron scattering factor. For the orbital scattering factors $f^X_{\text{Ne-core}}$, $f^X_{3s\text{-electron}}$, $f^X_{3p\text{-electron}}$ of S^{2-}, those calculated by Mann (1974) and summarized in *International Tables for X-ray Crystallography* (1974) were used. The curve denoted by *A-L* was obtained assuming the crystal potential of the Li_2S ionic crystal using an *ab initio* LCAO–Hartree–Fock calculation (Azavant & Lichanot, 1993). The curves for S^{2-} denoted by *S-W*, $R = 1.83$ and $R = 1.66$, were obtained using a Hartree–Fock calculation with a Watson sphere potential model, where the parameter R indicates the radius of the Watson sphere potential in Å (see Schmidt & Weiss, 1979). The curve for Zn^{2+} (Doyle & Turner, 1968) is also shown for reference.

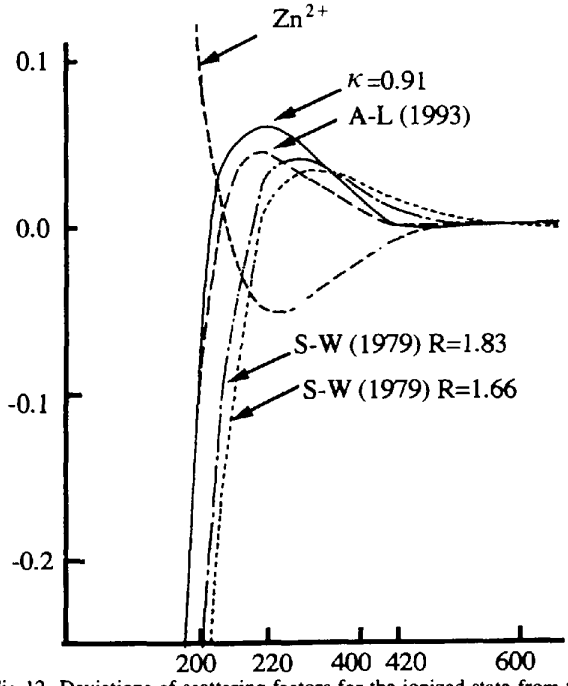

Fig 12. Deviations of scattering factors for the ionized state from the neutral state. The deviation of the scattering factor for Zn^{2+} is from Doyle & Turner (1968), which was obtained by a relativistic Hartree–Fock calculation. The deviation of the scattering factor for S^{2-}, denoted by $\kappa = 0.91$, was obtained from the Coppens model (Coppens *et al.*, 1979; Coppens, 1993) using the orbital scattering factors tabulated in *International Tables for X-ray Crystallography* by Mann (1974). The curve denoted by *A-L* is estimated for S^{2-} using the *ab initio* LCAO–Hartree–Fock calculation for an ionized Li_2S crystal by Azavant & Lichanot (1993). Curves denoted by *S-W* were obtained for S^{2-} by a Hartree–Fock calculation considering Watson-sphere potential models. *R* denotes the radius of the potential in Å.

Table 1. *Comparison of the U_{hkl} (Å^{-2}) derived experimentally and from other methods*

All U_{hkl} values in this table include temperature factors which were estimated by Cooper *et al.* (1973) and do not include the factor $(2\pi)^2$.

Reflection	DT* for neutral states	AL†	IT‡ for $\kappa = 0.91$	Present experiment§
200	0.003562	0.004961 [139%]	0.004355 [122.3%]	0.004363 (196) [122.5 (53)%]
220	0.037945	0.037900 [99.9%]	0.038113 [100.4%]	0.03822 (12) [100.7 (3)%]
420	0.004326	0.004277 [98.9%]	0.004148 [95.9%]	

* Calculated from the neutral scattering factor of Zn and S from the relativistic Hartree–Fock calculation, Doyle & Turner (1968). † The scattering factor of Zn^{2+} is from Doyle & Turner (1968) and that of S^{2-} is from Azavant & Lichanot (1993) using a LCAO–Hartree–Fock calculation and is labelled *A-L* in Fig. 12. ‡ The scattering factor of Zn^{2+} is from Doyle & Turner (1968) and that of S^{2-} is calculated from the orbital scattering factors of Mann in *International Tables for X-ray Crystallography* (1974), assuming $\kappa = 0.91$ using the Coppens model (Coppens *et al.*, 1979; Coppens, 1993). § Present experimental results. U_{220} was obtained from the critical-voltage effect of the 242 reflection at the [111] zone axis. U_{200} was obtained assuming that U_{600} was that of the neutral state and that for U_{420} was 0.5% smaller than the value for the neutral state. Quantities in brackets denote percentage values normalized using DT neutral states.

The curves in Fig. 12 show large deviations for lower scattering angles but they agree with the neutral state for higher scattering angles.

In Table 1, the calculated values for U_{200}, U_{220}, U_{420} and the experimentally derived values for U_{200}, U_{220} are shown. The first column gives values for neutral free atoms from Doyle & Turner (1968). In the second column, the ionized state Zn^{2+} is from Doyle & Turner (1968) and that for S^{2-} is from Azavant & Lichanot (1993). The third and the fourth columns were obtained by assuming $\kappa = 0.91$, for S^{2-} in the model by Coppens *et al.* (1979) and Coppens (1993), and Zn^{2+} is from Doyle & Turner (1967). The last column contains the analysis results of the experiments. U_{200} was obtained from the critical-voltage effect involving the 600 reflection in the [001] zone axis. In the analysis of this critical-voltage effect, U_{220} obtained from the critical-voltage effect of the $2\bar{4}2$ reflection at the [111] zone axis was used. Also, a value of U_{420} assumed to be 0.5% smaller than that for the neutral state was considered. From the experimental result for U_{200}, the parameter of Coppens *et al.* (1979) was derived to be $\kappa = 0.910\,(6)$ for the outer electrons of sulfur. Although better agreement for U_{200} is obtained with $\kappa = 0.900\,(10)$, we may conclude that the simple spherical model comprising an expansion of the outer-electron orbits can explain the measured low-angle structure factors with the value of κ being in the range 0.90 to 0.91. As seen in Fig. 12, the curve denoted by *A-L* has almost the same shape as the curve for $\kappa = 0.91$, but the latter is slightly larger. The curves

Table 2. *Comparison with the band-structure calculations in the form of X-ray structure factors*

All structure factors in this table do not include the temperature factors.

Reflection	DT* for neutral states	AL†	Present experiment‡	WK§ LCGO	BZ¶ PVMB	BZ** PVMB
200	13.32	13.14	13.17 (4)	13.06	13.01	13.04
220	31.76	31.78	31.66 (4)	31.54	31.47	31.48
400	26.50	26.60	-	26.35	26.28	26.26
420	9.316	9.377	-	9.24	9.19	9.21

*,† Same as the footnotes *,† in Table 1. ‡ To eliminate the temperature factors, the values obtained by Cooper *et al.* (1973) were used. Conversion from the scattering factor for electrons to that for X-rays was carried out using the scattering factor of Zn^{2+} obtained by Doyle & Turner (1968). § Linear combination of Gaussian orbital (LCGO) method using the local-density-theory of Wang & Klein (1981). ¶ Potential-variation mixed-basis (PVMB) method using the local-density theory by Bendt & Zunger (1982). ** Potential-variation mixed-basis (PVMB) method using the local-density theory by Bernard & Zunger (1987).

denoted by *S-W* do not agree well with the curve for $\kappa = 0.91$. A change in the Watson-sphere radius may give better agreement. Note that the scattering-factor curves in Fig. 12 for the deviation from the neutral state for the two ions show appreciable values at the 220 position. However, they tend to cancel as is confirmed experimentally by the value of U_{220} being only slightly different from that for neutral atoms.

In Table 2, the structure factors obtained from various band-structure calculations based on local-density theory are shown in the form of X-ray structure factors. The experimentally obtained scattering factors for electrons were converted to the scattering factors for X-rays using the Mott relation. The temperature factors were eliminated from the experimentally obtained structure-factor values by assuming the temperature factors of Cooper *et al.* (1973) and the scattering factor for Zn^{2+} of Doyle & Turner (1968). These assumptions appear to introduce no significant errors. The structure factors estimated from experiment and those obtained from Azavant & Lichanot (1993) are located midway between the results of the band-structure calculations and the neutral-state calculation. Although the values obtained by the band-structure calculations agree with each other, they seem to deviate from the experimentally derived values.

In the derivation of the U_{200} value, we assumed that the value of U_{420} for the ionized state was 0.5% smaller than that of the neutral state. If we assume the neutral-state value for the 420 reflection, a slightly smaller value for the X-ray structure factor of the 200 reflection will be given. On the other hand, if we assume a greater deviation in the value from the neutral state for the structure factor of the 420 reflection than that used for the present derivation, the X-ray structure factor of the 200 reflection will be increased towards that of the netural states. The experimentally derived value for the 200 structure factor will deviate from the values obtained by theoretical band-structure calculations shown in Table 2.

With various diffraction techniques, a small peak in the bonding charge density at a position between the two constituent atoms in binary semiconductor compounds has been detected (*e.g.* Demarco & Weiss, 1964; Collela, 1971; Bilderback & Collela, 1976; Kobayashi, Takama & Sato, 1988; Kobayashi, Takama, Tohno & Sato, 1988; Zuo, Spence & O'Keeffe, 1988; Spence, 1989). This bonding-charge peak, which can be expressed using a parameter $\rho_s(r)$ by García & Cohen (1993), influences the structure factor for the 400 reflection. The disagreements in Table 2 of the results obtained by various procedures for the 400 reflection can be attributed to this. However, the structure factors for the 200, 220, 420 and 600 reflections, which we used in the analysis of the critical voltage for the 600 reflection at the [001] zone axis, are not sensitive to this bonding-charge distribution. The structure factor for the 200 reflection depends on the total charge transfer between the two constituent atoms, which can be described by a parameter $\rho_A(r)$ introduced by García & Cohen (1993). Thus, the spherically symmetric model around the constituent atoms for the scattering factors can be used effectively in the present analysis.

6. Summary and conclusions

This study shows that even in a non-centrosymmetric structure several many-beam dyamical effects occur that are related to accidental Bloch-wave degeneracies. These effects are due to mirror or rotation symmetries in the three-dimensional or in the two-dimensional projected structure. At non-centrosymmetric projections, intensity anomalies similar to the critical-voltage effect occur. The second Bethe approximation was used to discuss this effect.

The observed accidental degeneracies of ZnS fell into three categories: those that could be used to derive accurate structure factors; those for which the structure factors could not be obtained with sufficient precision (high-voltage microscopes may solve this problem); and those expected to yield more information after further analysis. A series of the critical-voltage effects observed in the 260 reflection in the [001] projection and pseudo-critical-voltage effects in the non-centrosymmetric projections belong to the last category. As a result of the analysis of the critical-voltage effect observed in the $2\bar{4}2$ reflection at the [111] projection and that observed in the 600 reflection at the [001] projection, the structure factors for the 220 and 200 reflections, which have a large uncertainty in their scattering factors due to ionization, were derived. The analysis results were compared with various theoretical calculations.

APPENDIX *A*

From our previous work (Matsuhata & Gjønnes, 1994), the four-beam matrix can be rewritten as follows.

$$|\mathbf{A} - \gamma I| = 0,$$
$$XYZ + pX + qY + tZ + C = 0,$$

with

$$X = 2Ks_2 - \gamma + (U_{21}U_{12}/\gamma)$$
$$Y = 2Ks_3 - \gamma + (U_{31}U_{13}/\gamma)$$
$$Z = 2Ks_4 - \gamma + (U_{41}U_{14}/\gamma)$$
$$p = -[U_{31}U_{14}(1/\gamma + U_{43}/U_{13}U_{41})] \times \text{c.c.}$$
$$q = -[U_{41}U_{12}(1/\gamma + U_{24}/U_{14}U_{21})] \times \text{c.c.}$$
$$t = -[U_{21}U_{13}(1/\gamma + U_{32}/U_{12}U_{31})] \times \text{c.c.}$$
$$C = U_{12}U_{21}U_{13}U_{31}U_{14}U_{41}(1/\gamma + U_{43}/U_{13}U_{41}) \times (1/\gamma + U_{24}/U_{14}U_{21})(1/\gamma + U_{32}/U_{12}U_{31}) + \text{c.c.}$$

If $C^2 + 4pqt = 0$ and $X = -C/2p$, $Y = -C/2q$, $Z = -C/2t$, the degeneracy occurs. If a crystal has centrosymmetry, the four-dimensional matrix **A** (real and symmetric) always satisfies $C^2 + 4pqt = 0$. Even when a crystal is non-centrosymmetric, the Hermitian four-dimensional matrix **A** can satisfy $C^2 + 4pqt = 0$ if the crystal has a mirror plane or a rotation axis of even order.

References

Azavant, P. & Lichanot, A. (1993). *Acta Cryst.* A**49**, 91–97.

Bendt, P. & Zunger, A. (1982). *Phys. Rev. B*, **26**, 3114–3137.

Bernard, J. E. & Zunger, A. (1987). *Phys. Rev. B*, **36**, 3199–3228.

Bilderback, D. H. & Collela, R. (1976). *Phys. Rev. B*, **13**, 2479–2488.

Burns, G. (1977). *Introduction to Group Theory with Applications*, p. 311. New York: Academic Press.

Buxton, B. F., Loveluck, J. E. & Steeds, J. W. (1978). *Philos. Mag.* A**38**, 259–278.

Cochran, W. (1952). *Acta Cryst.* **5**, 630–635.

Collela, R. (1971). *Phys. Rev. B*, **3**, 4308–4311.

Cooper, M. J., Rouse, K. D. & Fuess, H. (1973). *Acta Cryst.* A**29**, 49–56.

Coppens, P. (1993). *International Tables for Crystallogaphy*, Vol. B, pp. 10–22. Dordrecht: Kluwer Academic Publishers.

Coppens, P., Guru Row, T. N., Leung, P., Stevens, E. D., Becker, P. J. & Yang, Y. W. (1979). *Acta Cryst.* A**35**, 63–72.

Demarco, J. J. & Weiss, R. J. (1964). *Phys. Lett.* **13**, 209–210.

Doyle, P. A. & Turner, P. S. (1968). *Acta Cryst.* A**24**, 390–397.

Fox, A. G. (1993). *Philos. Mag.* **68**, 29–37.

Fox, A. G. & Tabbernor, M. A. (1991). *Acta Metall. Mater.* **39**, 669–678.

García, A. & Cohen, M. L. (1993). *Phys. Rev. B*, **47**, 4215–4220.

Gevers, R., Serneels, R. & David, M. (1974). *Phys. Status Solidi B*, **66**, 471–482.

Gevers, R., Serneels, R. & David, M. (1975). *Phys. Status Solidi B*, **67**, 273–286.

Gjønnes, J. & Høier, R. (1971). *Acta Cryst.* A**27**, 313–316.

Gjønnes, J. & Taftø, J. (1993). *Ultramicroscopy*, **52**, 445–453.

Høier, R. (1969). *Acta Cryst.* A**25**, 516–518.

International Tables for X-ray Crystallography (1974). Vol. IV. Birmingham: Kynoch Press. (Present distributor Kluwer Academic Publishers, Dordrecht.)

Kambe, K. (1957). *J. Phys. Soc. Jpn*, **12**, 13–25.

Kästner, G. (1987). *Acta Cryst.* A**43**, 683–690.

Kobayashi, K., Takama, T. & Sato, S. (1988). *Jpn. J. Appl. Phys.* **27**, 1377–1380.

Kobayashi, K., Takama, T., Tohno, S. & Sato, S. (1988). *Jpn. J. Appl. Phys.* **27**, 1793–1797.

Mann, J. B. (1974). *International Tables for X-ray Crystallography*, Vol. IV, Table 2.2D, p. 108. Birmingham: Kynoch Press. (Present distributor Kluwer Academic Publishers, Dordrecht.)

Marthinsen, K., Matsuhata, H., Høier, R. & Gjønnes, J. (1988). *Aust. J. Phys.* **41**, 449–459.

Matsuhata, H. & Gjønnes, J. (1994). *Acta Cryst.* A**50**, 107–115.

Matsuhata, H., Gjønnes, J. & Taftø, J. (1994). *Acta Cryst.* A**50**, 115–123.

Matsuhata, H. & Steeds, J. (1986). *Philos. Mag.* B**55**, 39–54.

Moss, B., McMullan, R. K. & Koetzle, T. F. (1980). *J. Chem. Phys.* **73**, 495–507.

Pogany, A. P. & Turner, P. S. (1968). *Acta Cryst.* A**24**, 103–109.

Schmidt, P. C. & Weiss, A. (1979). *Z. Naturforsch. Teil A*, **34**, 1471–1481.

Serneels, R., David, M. & Gevers, R. (1975). *Phys. Status Solidi B*, **72**, 123–133.

Shannon, M. D. & Steeds, J. W. (1977). *Philos. Mag.* A**36**, 279–307.

Spence, J. C. H. (1989). Proceedings of EMAG89, pp. 155–158.

Spence, J. C. H. & Zuo, J. M. (1992). *Electron Microdiffraction*. New York: Plenum Press.

Taftø, J. & Gjønnes, J. (1985). *Ultramicroscopy*, **17**, 329–334.

Wang, C. S. & Klein, B. M. (1981). *Phys. Rev. B*, **24**, 3393–3416.

Watanabe, D., Uyeda, R. & Kogiso, M. (1968). *Acta Cryst.* A**24**, 249–250.

Zuo, J. M., Høier, R. & Spence, J. C. H. (1989). *Acta Cryst.* A**45**, 839–851.

Zuo, J. M., Spence, J. C. H. & O'Keeffe, M. (1988). *Phys. Rev. Lett.* **61**, 353–357.